CONFERENCES AND SYMPOSIA

Modern view of the solar wind from micro to macro scales

A A Petrukovich, H V Malova, V Yu Popov, E V Maiewski, V V Izmodenov,
O A Katushkina, A A Vinogradov, M O Riazantseva, L S Rakhmanova,
T V Podladchikova, G N Zastenker, Yu I Yermolaev, I G Lodkina, L S Chesalin

Contents

Abstract. **Solar wind — a plasma stream flowing out of the solar corona — is interesting both as a carrier of solar activity and as an example of a collisionless plasma. We present the main results of Russian studies in recent years. The original MHD model allows interpreting the bifurcation of the heliospheric current sheet during maximum activity years as occurring due to the quadrupole component of the heliomagnetic field. On a scale of the order of millions of kilometers, the solar wind consists of transient solar formations. On these scales, one of the basic geomagnetic forecast problems has been solved: it was shown that the interplanetary magnetic field can be assumed stable at times of about three hours. At small scales (hundreds to thousands of kilometers), local structures are formed that can be regarded, both individually and statistically, as turbulent cascades.**

A A Petrukovich [(1, a)], **H V Malova** [(1, 2)], **V Yu Popov** [(3, 4, 1)],
E V Maiewski [(4, 1)], **V V Izmodenov** [(1, 4, 5)], **O A Katushkina** [(1)],
A A Vinogradov [(1)], **M O Riazantseva** [(1)], **L S Rakhmanova** [(1)],
T V Podladchikova [(6)], **G N Zastenker** [(1)], **Yu I Yermolaev** [(1)],
I G Lodkina [(1)], **L S Chesalin** [(1)]

[(1)] Space Research Institute, Russian Academy of Sciences,
ul. Profsoyuznaya 84/32, 117997 Moscow, Russian Federation
[(2)] Lomonosov Moscow State University,
Skobeltsyn Institute of Nuclear Physics,
Leninskie gory 1, str. 2, 119991 Moscow, Russian Federation
[(3)] Lomonosov Moscow State University, Faculty of Physics,
Leninskie gory 1, str. 2, 119991 Moscow, Russian Federation
[(4)] National Research University Higher School of Economics,
ul. Myasnitskaya 20, 101000 Moscow, Russian Federation
[(5)] Lomonosov Moscow State University,
Faculty of Mechanics and Mathematics,
Leninskie gory 1, 119991 Moscow, Russian Federation
[(6)] Skolkovo Institute of Science and Technology,
Bol'shoi bul'var 30, str. 1, 121205 Moscow, Russian Federation
E-mail: [(a)] apetruko@iki.rssi.ru

1. Introduction

The solar wind is a stream of plasma (of the order of 10^9 kg s^{-1}) emanating the solar corona into interplanetary space, and composed mainly of electrons, protons, and helium nuclei (these last comprise $\sim 4\%$) [1–4]. It expels the interstellar plasma from the region of about 100 a.u., forming the heliosphere. The parameters of the stream (first and foremost, the velocity and density) are controlled by the magnetic field and transient features (mass ejections and fibers) above the Sun's surface.

The global quasistationary structure of the solar wind varies depending on the phase of the solar activity cycle [4–8]. The Sun's magnetic field is close to a dipole one at the cycle minimum. At high and moderate heliolatitudes, so-called coronal holes (seen as darker domains in UV photos) form, where the heliomagnetic field lines extend to infinity (Fig. 1a). A fast rarefied wind (with the speed ~ 700 km s^{-1}) escapes from them. Outside the coronal holes, the structure of the heliomagnetic field is more convoluted, and the field lines are closed. These zones are the sources of 'slow' wind (with the speed ~ 300–500 km s^{-1}). In years of maximum activity, the structure of the solar magnetic field becomes much more complex due to the appearance of a quadrupole component and higher-order multipoles. The coronal holes and zones of fast wind descend to lower latitudes, whereas zones of
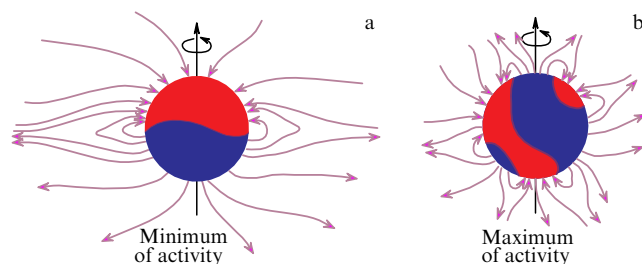

Figure 1. (Color online.) Schematics of the large-scale magnetic solar field: (a) a stretched quasi-dipole configuration at the cycle minimum and (b) a more complex multipole configuration at the maximum.
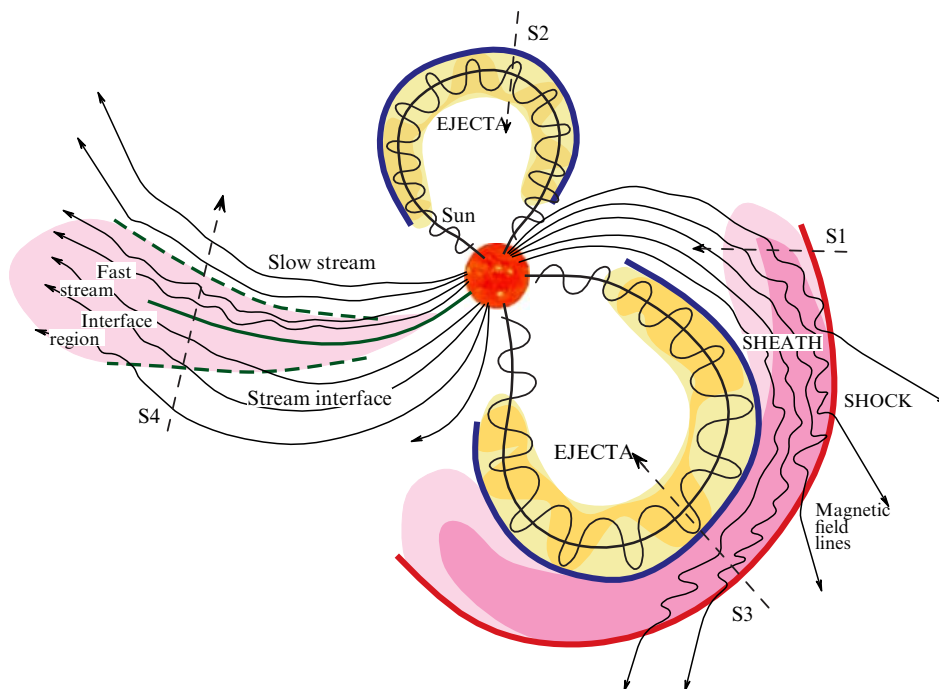
Figure 2. (Color online.) Schematic of solar wind structures caused by solar activity [6].

closed field lines and slow wind appear in high latitudes (Fig. 1b). This schematic structure and, in particular, the accompanying dependence of the solar wind speed on heliolatitude were confirmed by data from the spacecraft Ulysses [9–11].

The interplanetary magnetic field (IMF) is formed as a sum of the Sun's field and the field generated by current sheets that separate the zones of oppositely directed magnetic fields (outgoing from and incoming to the Sun in the individual hemispheres). As a whole, the large-scale solar wind can be described in the framework of magnetic hydrodynamics (MHD).

The speed of the solar wind is in fact constant (outside its acceleration zone in the close vicinity of the Sun, at about 10 million km), but varies depending on the wind's 'origin' from slightly less than 300 to 2000 km s^{-1}. The radial gradients of the density and magnetic field are simply governed by expansion. In Earth's orbit, the mean particle density is 6 particles (ions) per cm^3, and the magnetic field is 7 nT, and these values can vary by orders of magnitude (1–100 particles in cm^3 and 1–100 nT). Thermal and magnetic field energies are commonly only several percent of the directed motion energy. It takes the solar wind three days on average to reach Earth, and several months to reach the far extremes of the heliosphere. Large-scale wind fluctuations decay as they travel away from the Sun, and the wind becomes saturated with atoms and energetic plasma particles from the interstellar space.

On scales of the order of millions of kilometers (which correspond to spacecraft observation intervals from tens of minutes to tens of hours), the solar wind stream is dominated by remnants of various transient solar structures. 'Ordinary' solar wind variations are typically of the order of twice the mean values. Such a solar wind can nevertheless generate rather strong geomagnetic activity in the near-polar zone (so-called magnetic substorms and polar auroras) under appropriate conditions [11, 12].

In addition, relatively stable and extended magnetic plasma structures related to the manifestations of solar activity are formed episodically. In the region where the fast and slow streams of the solar wind (generated in the respective regions of open and closed magnetic fields on the Sun) come close to each other, a so-called corotating interaction region is formed (Fig. 2), which can rotate together with the Sun for months, and is characteristic of the phase when solar activity is decreasing or at a minimum. It is characterized by a high plasma concentration in excess of 10 cm^{-3} and a fluctuating magnetic field exceeding 10 nT [8, 13]. The period of the solar maximum is accompanied by coronal mass ejections mainly related to solar flares. Magnetic clouds that are then formed in the heliosphere can move relative to the calm (background) solar wind at speeds up to 2000 km s^{-1}, carrying a highly structured magnetic field (commonly twisted into a bundle) of tens of nT. Fast magnetic clouds, just like fast streams in the corotating interaction region, can compress the plasma of the unperturbed solar wind ahead of them; and if the ejection speed exceeds the speed of the background stream by more than the local speed of sound, a shock wave is formed at the front, with the magnetic field behind it enhanced by compression. Magnetic clouds and corotating interaction regions cause global perturbations of the geomagnetic field, magnetic storms [14], the most powerful ones being associated with the structures occurring when two or more such objects collide [15–17].

The dynamic pressure of the solar wind forms a comet-shaped structure of the magnetosphere from Earth's dipole magnetic field. However, the main factor determining the dynamics of the magnetosphere is the IMF. The components of the IMF lying in the plane of the ecliptic are largely shaped by the large-scale spiral structure of the IMF, while the vertical component is less constrained and hence less predictable. The electrodynamic link between the solar wind and the magnetosphere is mainly governed by the transverse electric field $E_y = VB_z$, with only negative values of B_z,

directed opposite to Earth's magnetic field, being geo-effective. Here, the geo-solar-magnetospheric coordinate system is used, with the origin at Earth's center, the x axis directed to the Sun, and the z axis deflecting from the zenith direction synchronously with the direction of the geomagnetic dipole [18].

On scales from tens to thousands of kilometers (seconds and minutes in spacecraft observations), comparable to characteristic times and lengths of the plasma medium (the proton gyroradius is several hundred km, and the gyroperiod is larger than 10 s), solar wind is commonly treated in terms of local plasma dynamics. This is an essentially collisionless plasma (a characteristic mean free path is comparable to the distance between Earth and the Sun) dominated by the stream kinetic energy, with a developed structure of density and magnetic field fluctuations [19–21].

From the standpoint of experimental physics, solar wind is an extremely rarefied medium, which is irreproducible in a terrestrial laboratory. Remote sensing of its large-scale structure in the 'near field' (several dozen million km from the Sun) is possible using glowing in white scattered light or the radio transillumination method. Remote sensing of the far heliosphere and, in particular, of the parameters of the interstellar medium is possible using the data on streams of cosmic rays, neutral atoms, and the UV glow.

The solar wind is locally monitored by spacecraft. It was first detected by Soviet interplanetary stations Luna-1 and Luna-2 in 1959 [22], only a few years after the first suitable theory of solar corona expansion was proposed [23]. Since then, measurements in Earth's orbit have been carried out with dozens of spacecraft. Beginning in 1997, spacecraft providing continuous monitoring of the solar wind have operated at the forward Sun–Earth libration point at the distance of 1.5 million km from Earth's magnetosphere. The solar wind in interplanetary space is observed using specialized spacecraft or those that fly by (on their way to planets) in essentially the entire range of distances to the Sun (0.3 a.u., which is 50 million km in the Ulysses mission) up to the boundary of the heliosphere (Pioneer and Voyager spacecraft). The Parker Solar Probe launched in 2018 is scheduled to approach the Sun to a record 10 million km.

The standard set of measurements on a spacecraft includes the measurement of the (permanent) magnetic field, energy and velocity distribution functions for ions and electrons, the mass ion composition, and plasma waves (varying electromagnetic fields) up to the maximum possible plasma frequency. The basic methodological problem of local measurements is that they are related to the concrete time and space position of the spacecraft. The actual spatial distribution of any parameter cannot be obtained from measurements on an individual spacecraft without additional assumptions. Given the apparent lack of knowledge of the spatial structure, numerical simulations of all relevant aspects acquire utmost importance, ranging from the solar corona formation to interactions between the solar wind and interplanetary medium.

This review briefly presents the main new results of Russian research dealing with the global solar wind structure and problems of geomagnetic activity forecast based on measurements of the IMF and local plasma variations.

2. Global quasistationary structure

The key elements of the global structure of the heliosphere (in years of low solar activity) are the regions of fast solar wind

with the magnetic field directed oppositely at the poles, and the region of slow solar wind in low latitudes. The latter is frequently referred to as a heliospheric plasma sheet [24, 25] because of the increased plasma density. It 'encases' a much thinner heliospheric current sheet (HCS) [26] that separates regions of different magnetic field polarities. It is supposed that the HCS is a continuation of the streamer belt framing the neutral line in the solar corona [27–32].

The HCS structure can evolve following the 22-year solar activity cycle [33, 34], when the dipole harmonics of the heliomagnetic field alternate with the quadrupole ones. In years of minimum solar activity, the HCS is predominantly observed in low latitudes (in the $\pm 15°$ latitude belt), but in periods of maximum activity it can deviate from the equatorial plane by $50° - 70°$ or more [30, 35]. Observations of the HCS in high latitudes are frequently interpreted as indications of the existence of several HCSs of conical shape in the northern and southern hemispheres [36, 37]. A relatively small number of papers are devoted to modeling the heliosphere taking the quadrupole magnetic field into account, and most of them are semi-empirical [36–39]. They regard the possibility of the existence of two HCSs as a consequence of the nondipole heliomagnetic field.

In order to specifically explore the large-scale quasistationary structure of solar wind viewed as a self-consistent system of electric currents and magnetic fields, an MHD model of the heliosphere has been developed [40]. With its assistance, the position of global current sheets in different phases of the solar cycle could be explored in detail. The boundary conditions for the model with the contributions from dipole and quadrupole components of the Sun's magnetic field are specified for a sphere of the radius $20R_S$ (R_S is the radius of the Sun), where the stream is already supersonic, and smaller-scale structures in the corona are discarded.

The solution has the following power-law asymptotic behavior as $r \to \infty$: $V_r \sim 1$, $V_\theta, V_\varphi \sim r^{-1}$ for the plasma velocity, $B_r \sim r^{-2}$, $B_\theta \sim r^{-3}$, $B_\varphi \sim r^{-1}$ for the magnetic field components, $J_r \sim r^{-2}$, $J_\theta, J_\varphi \sim r^{-3}$ for the current densities, $P \sim r^{-10/3}$ for the plasma pressure, $\rho \sim r^{-2}$ for the density, and $T \sim r^{-4/3}$ for the temperature. These asymptotic forms agree with estimates obtained earlier using highly simplified systems of equations [41–45].

Figure 3 shows two-dimensional distributions of the components of the Sun's magnetic field B_r, B_θ, and B_φ for three ratios of the quadrupole component to the dipole one, $\tau = 0$, 0.5, and 1, which respectively correspond to the solar minimum, an intermediate state, and the solar maximum. The distributions of the plasma density ρ for $\tau = 0$ are shown in Fig. 4. The axes z and x, expressed in units of R_S, are respectively directed along the solar magnetic moment and along the equator. For the dipole magnetic field ($\tau = 0$), the HCS (detected by the sign change in the radial magnetic field) is located in the equatorial plane; all distributions are symmetric in both hemispheres. As the contribution of the quadrupole component increases, a conical neutral sheet forms in the near-polar region of the southern hemisphere and moves toward the low latitudes; simultaneously, the 'main' HCS shifts to higher latitudes (Fig. 3d, e, f) in the northern hemisphere. For a purely quadrupole field, the two HCSs become similar, being located at $30°$ to the equatorial plane (Fig. 3g, h, i). The density distribution in the maximum activity period (see Fig. 4) has a characteristic form with
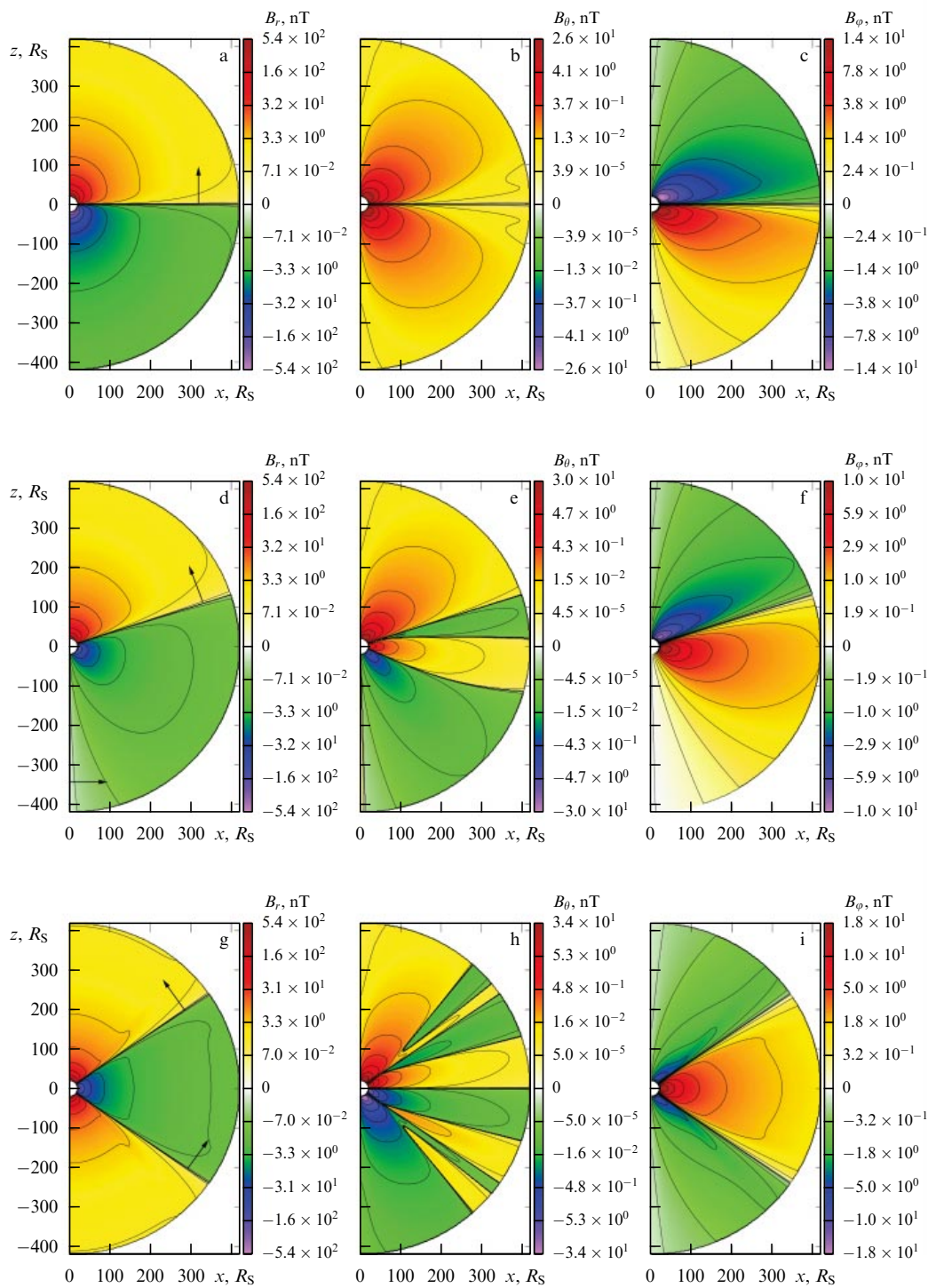
Figure 3. (Color online.) Maps of distributions of the magnetic field components B_r, B_θ, and B_φ for various values of the relative contribution from the quadrupole magnetic field component $\tau = 0$ (a, b, c), 0.5 (d, e, f), and 1 (h, g, i). The vertical z axis is codirected with the Sun's rotation axis, the horizontal x axis lies in the equatorial plane. The arrows show the direction of current sheet displacement with an increase in τ. The color codes the amplitude of the magnetic field, expressed in nT.

two maxima in mid-latitudes where the HCSs are located. As the Sun's magnetic field evolves further, the northern HCS ascends to higher latitudes and disappears (the arrows indicate the displacements of current sheets over the latitude), and the new southern sheet moves to occupy the standard equatorial position, with the direction of the Sun's magnetic field being reversed.

The existence of an HCS in high latitudes was confirmed by measurements made by Ulysses at the distance of two to three astronomical units from the Sun; however, its structure proved to be substantially more complicated. Long-lived current sheets of conical (or cylindrical) shape were discovered in years of minima in coronal holes over the Sun's south pole [46] (Fig. 5). Inside the high-latitude conical current
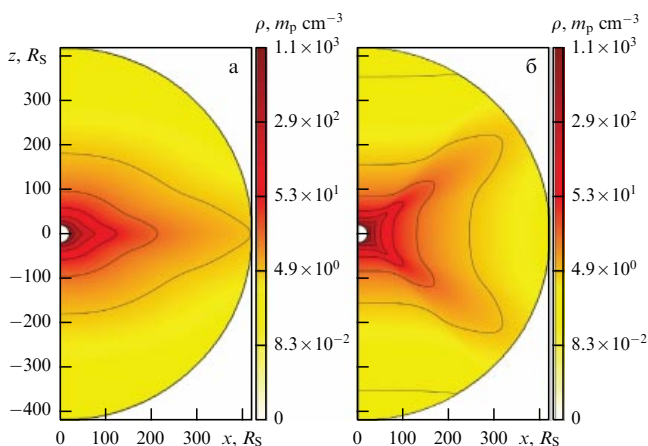
Figure 4. (Color online.) Distribution of the plasma density ρ in the vertical section of the heliosphere for (a) $\tau = 0$ and (b) $\tau = 1$ in the maximum activity case (analogous to Fig. 3)
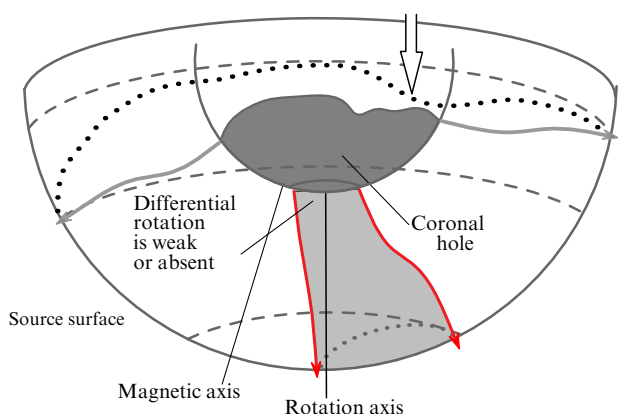

Figure 5. Polar conical current sheet in the heliosphere (adapted from [46]).

sheet, the solar wind is slower and denser than outside. The data from Ulysses agree with the results of computational reconstruction of the sheet structure by the heliomagnetic field [44] and also with drops in solar wind velocity inside fast streams from coronal holes by observations of interplanetary

scintillation in the same periods. The discovery of such high-latitude structures opens new perspectives for the understanding of the role of the high-latitude heliosphere as a whole. In particular, it has been shown that solar cosmic rays can propagate along them.

Remote monitoring of the global structure of the heliosphere can be carried out by measuring the Lyman-alpha radiation scattered on interstellar hydrogen atoms [47]. Interstellar hydrogen atoms penetrate the heliosphere from the interstellar space owing to their large mean free path. Their distribution is affected by solar gravity and radiation pressure, as well as by charge exchange processes with solar wind protons and photoionization, which lead to a loss of atoms as they approach the Sun.

Charge exchange is the main process leading to the loss of interstellar atoms in the vicinity of the heliopause and within the heliosphere at heliocentric distances of 1–3 a.u. An atom born in a charge exchange preserves the speed of the solar wind, about 400–800 km s^{-1}, and cannot scatter solar Lyman-alpha photons. The intensity of scattered radiation is proportional to the hydrogen atom concentration, which is in turn determined by the mass flux of the solar wind. The larger the mass flux, the higher is the atom charge exchange rate and hence the lower their concentration and the intensity of Lyman-alpha radiation scattered on atoms.

By making celestial maps of the intensity of scattered Lyman-alpha radiation and solving the inverse problem, we can reconstruct the dependence of the solar wind mass flux on heliolatitude [48–51]. Figure 6 shows the dependence of the solar wind mass flux and concentration on the heliolatitude and time based on measurements of scattered Lyman-alpha radiation on the SOHO spacecraft (with the SWAN instrument) in 1996–2017 [50]. The concentration is obtained from the mass flux using the solar wind speed known from measurements of interplanetary scintillations [52]. During the periods of solar minima, 1996–1997 and 2009–2010, the dependence of concentration on heliolatitude corresponds to the standard one: the maximum of the solar wind concentration in the region of the Sun's equator and minima at the poles. However, concentration maxima are clearly seen at mid-latitudes of $\pm 30 - 50°$ near the solar maximum in 2002–2005. At the solar maximum of 2014–2016, these concentration peaks are less prominent, which
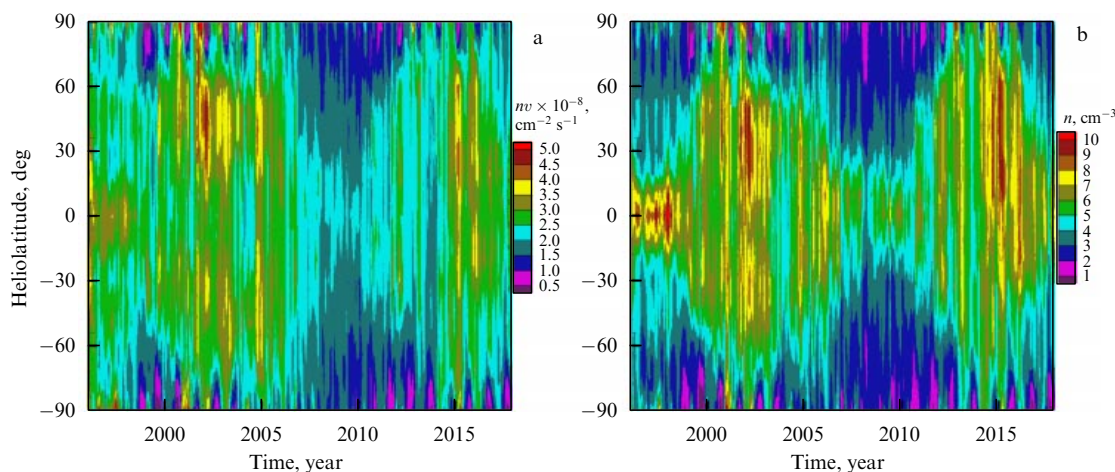

Figure 6. (Color online.) Dependence of (a) the mass density flux and (b) the concentration of solar wind at 1 a.u. on time and heliolatitude. The results are obtained by analyzing the data from SOHO/SWAN on scattered Lyman-alpha radiation [50].

can be related to weaker solar activity in the 24th solar cycle than in the 23th.

A comparison of observational data from the SOHO spacecraft with the results of MHD modeling discussed above shows a qualitative agreement between theoretical and experimental results; therefore, to explain the presence of two density maxima, it suffices to have a heliomagnetic field with a dominant quadrupole component during the solar maximum.

3. Mesoscale transient structures in solar wind and their forecast

One of the most pressing problems in solar wind research is the computation and forecast of the dynamics of the magnetosphere and ionosphere. A numerous empirical and physical models have been developed that translate characteristics of solar wind and the interplanetary magnetic field into parameters of the ionosphere and magnetosphere. A forecast can be made, for example, if a spacecraft observing the solar wind is located 'upstream' from Earth. For a longer forecast period, the spacecraft should be as distant from Earth as possible. The most convenient place is the forward libration point in the Sun–Earth system, about 1.5 million km from Earth, where a spacecraft can stay continuously without large fuel consumption. Since 1997, the US ACE spacecraft on a halo orbit with a radius of 200,000 km has been continuously transmitting solar wind and IMF measurement data in real time. Since 2018, operational data has been coming from the DSCOVR satellite. The forecast time relies on the difference between the speeds of radio signals and the solar wind, being about one hour for a wind speed of 400 km s^{-1} and about 20–30 min for high-speed streams. This forecast scheme, even though it has become classical, nevertheless faces a number of fundamental problems.

The first problem is to estimate the accuracy of the acquired characteristics of the solar wind and the IMF taking natural spatial variability of interplanetary space into account. A spacecraft should be close to the Earth–Sun line to increase the forecast fidelity. The variability can be estimated by comparing simultaneous measurements from several satellites. Generally, the distance between satellites transverse to the Earth–Sun line, at which the correlation between measurements drops substantially and hence the quality of the forecast deteriorates, is about 400,000–1,000,000 km [53, 54]. And yet the results of correlation analysis are insufficient for concluding to what degree these differences are important for the forecast fidelity.

In this respect, for comparison, it is more relevant to deal with a function of the solar wind and IMF parameters that could also characterize the impact on the magnetosphere (the so-called transfer function) [55]. For example, one may choose the epsilon parameter — the Poynting vector for the electromagnetic energy penetrating into the magnetosphere [56]. Simultaneous solar wind measurements on the near-Earth spacecraft Interbol-1 and the Wind spacecraft located in the vicinity of the libration point or on transient orbits at a long distance from Earth (more than 5000 h in 1995–1999) were used for such a comparison. Two quantities with the dimension of energy were computed: E_2, which is the integral of the epsilon parameter over 90 min, characterizing ordinary geomagnetic variability (substorms) and E_1, which is the integral of the epsilon parameter over the time interval when this parameter is larger than 5×10^9 W, characterizing
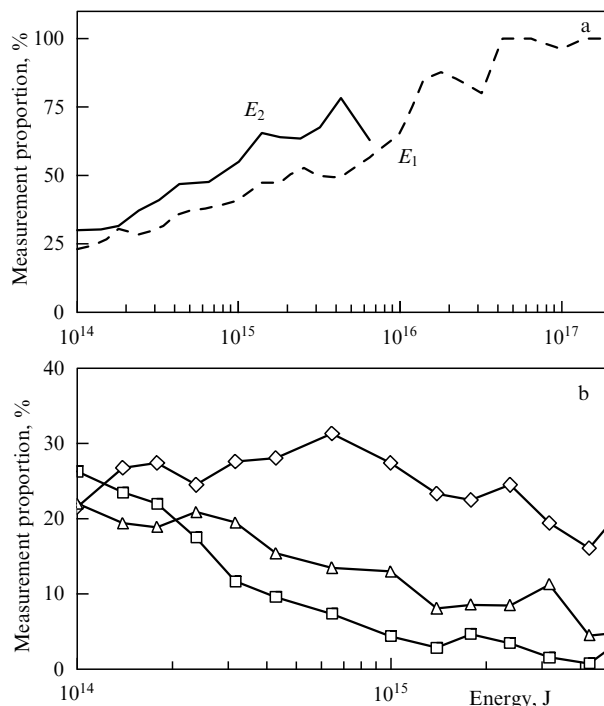

Figure 7. (a) Fraction of measurements with a difference of less than 15%. E_1 is the energy accumulated during the interval with power not less than 5×10^9 W; E_2 is the energy accumulated for the 90 min interval. (b) Proportion of different values of E_2 as a function of the difference (diamonds — 10–15%, triangles — 30–50%, squares — more than 50%).

magnetic storms. The relative difference between measurements on these two satellites, R, was computed (Fig. 7). The measurements were treated as coinciding if $R < 0.15$. In the E_2 energy range 10^{14}–5×10^{15} J, the fraction of observations that coincide increases from 30 to 80%. For E_2 equal 10^{15} J (a moderately strong substorm), the error exceeds 0.3 in 25% of cases. At energies that correspond to a magnetic storm ($E_1 > 10^{16}$ J), the data from two spacecraft practically coincide. Such a dependence of the fraction of differing measurements on the energy level has a natural explanation: high energies correspond to large-scale structures of solar wind with a characteristic size much larger (millions of km) than possible distances between the satellites. The solar wind structure causing substorms is mainly related to smaller-scale Alfvén variations, and the problem of forecast accuracy is much more acute for them.

The second problem is the physical sustainability of the forecast computed in advance with respect to the solar wind used. The natural lag of several dozen minutes ensured by the separation between the spacecraft and Earth is insufficient for many practical problems. A 'longer' forecast in fact relies on the assumption of a future solar wind and on the inertia in the dynamics of the forecast subject (for example, the geomagnetic index). Both elements are important, because the inertia is capable of compensating inaccuracies in the knowledge of the future wind to a substantial degree. Thus, the achievable forecast length can differ depending on the parameters being forecast. We illustrate the problem with a computationally undemanding forecast of the geomagnetic index Dst, which characterizes the net amplitude of a magnetic storm [57, 58].

The development of a magnetic storm is a gradual process that can occupy several hours after the first contact between

the magnetosphere and an interplanetary perturbation (negative vertical component of the IMF). The empirical model used for the forecast [59, 60] has the form

$$\frac{d\text{Dst}^*}{dt} = Q(t) - \frac{\text{Dst}^*}{\tau}, \qquad (1)$$

$$Q(t) = -4.4(VB_s - 0.5),$$

$$VB_s = \begin{cases} |VB_z|, & B_z < 0, \\ 0, & B_z \geqslant 0, \end{cases}$$

$$\tau = 2.4 \exp \frac{9.74}{4.69 + VB_s},$$

where V [km s^{-1}] is the solar wind speed and $B_s (nT)$ is the southward component of the IMF. The characteristic time τ defining the inertia is related to losses in the inner magnetosphere and decreases as the solar wind effect becomes stronger. In this model, τ is in the range from ten hours for weak storms to three hours for strong storms.

The only sufficiently universal assumption that can be made about the future solar wind behavior is that its characteristics remain constant on the level of current values after the arrival of a large-scale solar wind perturbation due to solar activity is detected. An alternative can be the use of some model form for perturbations (for example, a magnetic bundle for magnetic clouds [61]). However, 'ideal' isolated structures are observed rather seldom; furthermore, the strongest storms are triggered by structures of complex composition. A suitable duration under the constancy assumption can be determined only statistically.

The forecast model was based on Eqn (1), which, for a constant solar wind, predicts the geomagnetic index approaching the asymptotic value equal to $Q\tau$. A statistically substantiated forecast of the peak of the Dst index (deviation of the forecast from the observed value not greater than 25% for 80% of magnetic storms) is specified by the following empirical algorithm.

1. The index expected in three hours is computed assuming a constant Q. This forecast is refreshed every hour.

2. Upon registering a sufficiently sharp and strong jump in the parameter Q, the expected storm amplitude equal to the saturation value $Q\tau$ is additionally computed. As a rule, such jumps occur once or twice during stronger storms.

3. Exact criteria for the 'jump strength' and other additional empirical parameters of forecast are given in original study [57].

As follows from the analysis, this method fails to provide a realistic forecast for the registration time of the index peak value (on average, up to 10 hours before the onset of the storm) and for the temporal index profile. In fact, making the forecast rougher (by estimating only the storm peak instead of the temporal profile) is the price to be paid for earlier notification.

A forecast of this type proved to be more productive for stronger storms (with the peak value Dst < –100 nT). Their beginning is typically accompanied by a sharp jump in solar wind parameters, and the saturation time is close to the lower bound (about three hours). For such a short time interval, the assumption that solar wind is constant is sufficiently reliable, which allows making a suitable forecast for the storm amplitude at the very beginning. The natural reasoning that stronger perturbations of the interplanetary medium have a larger spatial scale also plays its positive role.
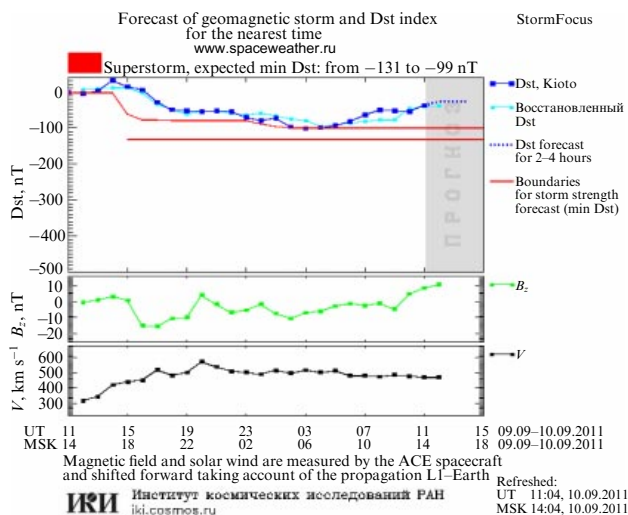

Figure 8. (Color online.) Screenshot of the forecast of a strong magnetic storm in 2011. The red lines in the top panel show the forecast values of the storm peak based on the solar wind jump (lower line) and the running three-hour forecast (upper line).

The peaks of practically all small storms in the range $-50 > \text{Dst} > -100$ nT can be predicted only on the basis of a three-hour forecast updated in the course of the storm. The expected values of index saturation are practically never achieved, because the assumption that the solar wind is constant is not valid for long saturation times (about ten hours), and the perturbation interval can already end. Thus, as follows from this analysis, the assumption that the magnetic field of the solar wind is constant can be valid for a period of not more than several hours, which sets physically grounded bounds for forecasting magnetic storm amplitudes.

Based on this method, the service StormFocus (http://spaceweather.ru), forecasting geomagnetic storms, was launched on the site of the Institute for Space Research RAS in 2011; it provides a reliable forewarning of the probable strength of a geomagnetic storm in the next several hours. An example of a forecast of a strong storm is shown in Fig. 8.

4. Small-scale variations in the solar wind and the interplanetary magnetic field

Variations in the solar wind on small scales, comparable to the characteristic plasma lengths, can also be interpreted as turbulence, i.e., as a hierarchy of objects such that none of them can be analyzed individually in terms of physical processes, and also as a set of coherent structures, each with its own internal arrangement. Variations in the IMF have been studied the most [62].

In a considerable number of observations of the IMF, its structures can be classified in terms of discontinuities — stationary MHD solutions [63] that include rotational discontinuities, tangent discontinuities, and shock waves. The first two types, encountered most frequently [64, 65], can rarely be distinguished because of experimental difficulties in reconstructing the local coordinate system based on the single-spacecraft observational data [66, 67]. The importance of this problem is related to the generation mechanism. Rotational discontinuities, in accordance with our present understanding, are formed via steepening of Alfvén waves propagating in an inhomogeneous plasma [68–70]. Tangential

discontinuities are probably formed at the boundaries of solar wind streams with different velocities [71, 72]. We present results of some recent studies as examples of the analysis of such individual structures.

Observations of a discontinuity with several satellites, for example, four Cluster spacecraft [73], allow using the time delays to reconstruct the propagation direction of the discontinuity and the velocity in the normal direction by temporal delays and hence to determine spatial scales of magnetic field variation and the electric current density. For discontinuities, a local coordinate system can be introduced (where B_l corresponds to the direction of the maximum field change, B_n to the direction along the normal to the discontinuity plane, and B_m to the direction along the main component of the current density), and the spatial distribution of two components of the electric current density $j_m = (c/4\pi)\,\partial B_l/\partial n$ and $j_l = -(c/4\pi)\,\partial B_m/\partial n$ can be reconstructed. It is assumed that the discontinuity is a locally one-dimensional current sheet, with $j_n = 0$. Figure 9 shows the current density component along the magnetic field, $j_\parallel = (j_l B_l + j_m B_m)/B$, and that perpendicular to the magnetic field, $j_\perp = (j_l B_m - j_m B_l)/B$. The current amplitude reaches several tens of nA m^{-2}, which considerably exceeds earlier estimates of current intensity derived from single-satellite measurements [74, 75]. The current is localized on scales of the order of several ion inertial lengths $d_i = c/\omega_{pi}$, where ω_{pi} is the ion plasma frequency. The presence of a nonzero B_n component indicates that we must be dealing with a rotational discontinuity. The main current flows along the magnetic field, and therefore such a current sheet represents a forceless configuration. The amplitude of the magnetic field B_m is comparable to the field amplitude B_l, whereas the spatial distribution of B_m corresponds to $B_l^2 + B_m^2 \approx$ const, such that the magnetic field hodograph has the form of an 'arch' (see Refs [76–78] for models of such configurations).

Statistics of observations of such structures comprise about 100–200 events per day. Their stability can be estimated by comparing data from spacecraft located sufficiently far, but still at a distance where the observation of the same discontinuity can be unequivocally confirmed. A comparison of the data from the spacecraft ARTEMIS [79], orbiting the Moon at a separation of $\sim 4 \times 10^5$ km from Earth, and MMS [80], on an orbit with an apogee of $\sim 1.6 \times 10^5$ km, indicates that at a distance $\sim 2 \times 10^5$ km, there is no essential deformation or breakup of the structure of discontinuities [81]. The discontinuity propagation time is 10 to 15 min, which is several orders of magnitude greater than the characteristic time of the dynamics of solar wind ions (gyroperiod), which is a robust estimate for the development time of plasma instabilities [82, 83]. These results call for theoretical reevaluation of processes whereby discontinuities form and interact with solar wind ions.

In general, the correctness of structure classification based on MHD models of discontinuities (tangent of rotational) may cause doubts. For a substantial part of observed discontinuities, a jump in the tangential speed of electrons is noted, which makes 70% of the jump of the Alfvén velocity (these jumps should be equal according to the Walén relation), which says something about the nongyrotropy of the pressure tensor in the plasma and hence about the kinetic nature of the given structure [76]. On the other hand, an alternative classification is possible, viewing discontinuities as current sheets with a different distribution of the plasma pressure and the magnetic field. We have discovered three
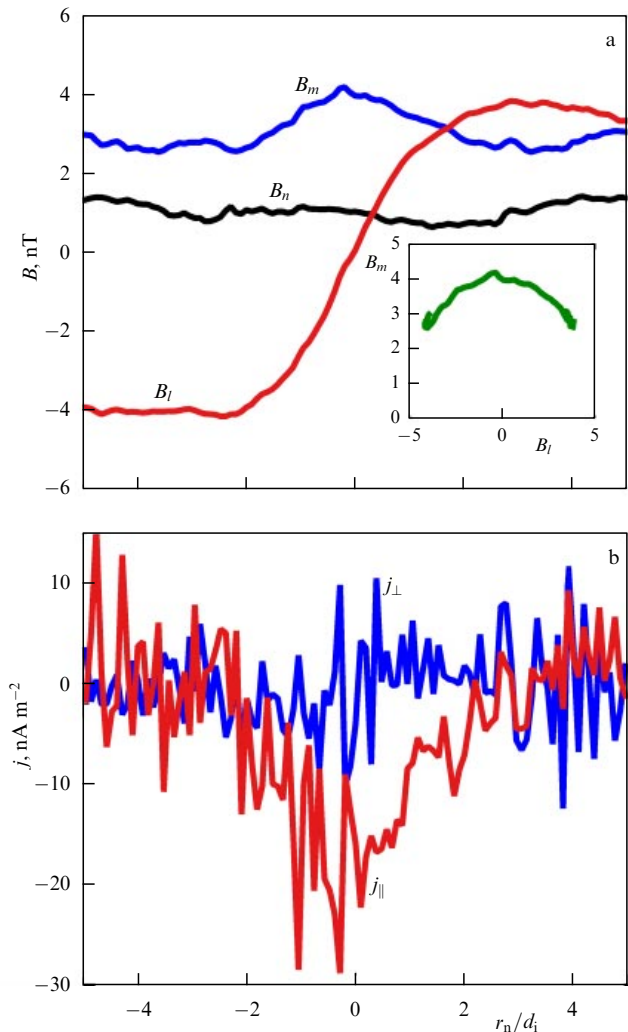

Figure 9. (Color online.) (a) Three magnetic field components and (b) two components of current density as functions of a coordinate along the normal to the discontinuity plane. The spatial scale is normalized to the ion inertial length d_i.

types of sheets: with a magnetic pressure minimum at the center, with a magnetic pressure maximum at the center, and with different magnetic pressures in front of and behind the sheet. In the majority of observed cases, the variation in pressure is due to the variation in the plasma density at a constant temperature.

In the alternative approach, the entire set of magnetic field and plasma oscillations can be regarded as a hierarchy of structures embedded into each other and interacting with each other, and described using the methods of spectral or correlation analysis [84–90]. Such approaches play an important role in describing energy transport (albeit in a strongly averaged form), heating, and particle acceleration [91].

The presence of structures across a wide range of scales, which together form a turbulent cascade, makes the solar wind a convenient laboratory for exploring turbulence in a collisionless plasma. Taylor's hypothesis [92] (that stationary structures drift at the speed of the solar wind) allows directly identifying temporal variations of parameters measured by spacecraft with spatial variations used in theory. Generally, there are three characteristic scales in the turbulent cascade of the solar wind [89]. At the largest scales, which reflect the

large-scale structure of the solar corona, the energy is pumped into the system (through injection of large-scale objects carrying excess energy, such as a jump in velocity, density, temperature, and magnetic field); at intermediate scales, filled with various MHD structures (mainly Alfvén waves [93] and magnetic tubes [94]), energy is transferred from larger to smaller scales (so-called inertial or MHD scales, in fact, the dynamics of boundary layers); and, finally, at small scales, with variations generated as the result of evolving plasma instabilities on ion and sub-ion scales [95] due to the steepening of the boundaries of magnetoplasma objects, with energy being dissipated into the thermal energy of particles (the so-called dissipative of kinetic scales).

Recently, the so-called ion–kinetic scales (of the order of the ion gyroradius or ion inertial length: 10–1000 km, commonly 50–100 km) have been discussed in both theoretical and experimental studies; on those scales, the energy dissipation into plasma heating is most efficient. The related observational studies for a long time were predominantly based on measurements of the IMF [96]; the reason was the sparsity of the measurements of plasma parameters at a sufficiently high sampling rate [97, 98]. In the last decade, the spectrometer BMSW deployed aboard the Spektr-R spacecraft as part of the PLAZMA-F experiment [99–101], has been measuring the solar wind stream with a temporal resolution of 31 ms. This for the first time enabled systematic measurements of the ion stream and plasma density and velocity on ion and sub-ion scales (see, e.g., [102–106]). As a result, temporal resolution of plasma measurements was improved by almost two orders of magnitude.

Figure 10 presents an example of a typical spectrum of fluctuations of the solar wind ion stream based on measurements by the BMSW spectrometer (see also [104]). At frequencies of 0.02–1 Hz, the spectrum decays as a power law with the slope ~ -1.6, which is close to the mean slope observed for fluctuations of the IMF on inertial scales [89, 96]. These values correspond to Kolmogorov's $-5/3$ scaling predicted for fluctuations that are perpendicular to the mean magnetic field direction, which dominate in the collisionless plasma of the solar wind [107]. At higher frequencies, the spectrum steepens to the slope ~ -2.7, which also on average corresponds to the slope of IMF spectra. This value exceeds (in absolute value) the slope $-7/3$ predicted by the theory of kinetic Alfvén turbulence [108] and approximately corresponds to the exponent $-8/3$ obtained taking the spatiotemporal turbulence inhomogeneity [109] or Landau damping [110] into account. The break in the spectral slope in Fig. 10 is observed at a frequency of ~ 1.2 Hz, which is in this case close to the transfer frequency that corresponds to the thermal proton gyroradius $F_{\rho i} = V/2\pi R_{\mathrm{T}} = 1.3$ Hz (where $V = 334$ km s^{-1} is the stream velocity, $R_{\mathrm{T}} = V_{\mathrm{th}}/\omega_{\mathrm{c}} = 40$ km is the thermal proton gyroradius, $V_{\mathrm{th}} = 18$ km s^{-1} is the thermal proton velocity, and $\omega_{\mathrm{c}} = 0.45$ rad s^{-1} is the cyclotron frequency). This agrees with the view that the break in the spectral slope reflects a transition from incompressible Alfvén to kinetic Alfvén turbulence [108]. However, statistics do not show that the break frequency corresponds to some unique plasma scale [103, 111]. This can be explained by the deviation of turbulent regimes from model ones. The theoretical approaches described above were proposed for homogeneous developed turbulence, with statistical characteristics independent of the way energy enters the system [107]. Such approaches ignore the inhomogeneity of the distribution often observed in the solar wind.
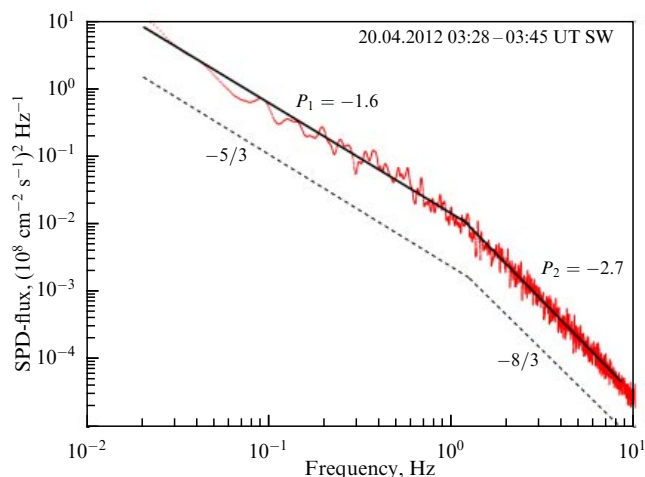

Figure 10. Spectrum of ion flux fluctuations as measured by the BMSW instrument. P_1 and P_2 are the spectral slopes on the respective inertial and kinetic scales. The dotted lines correspond to the predictions of turbulence theory. SPD is the spectral power density.
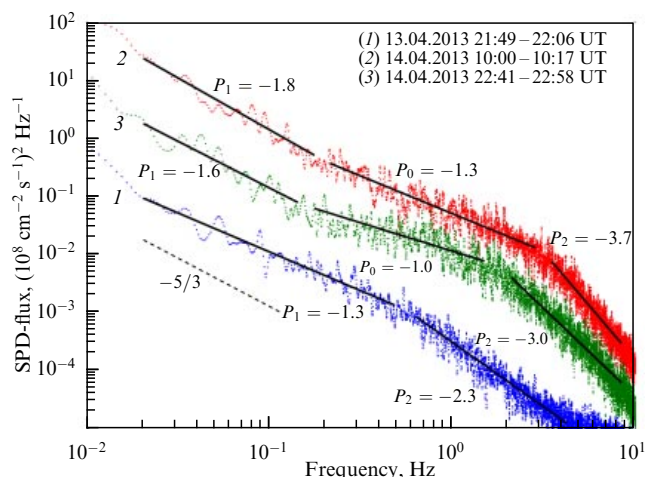

Figure 11. (Color online.) Comparison of the ion flux fluctuation spectra based on measurements by the BMSW instrument for successive intervals: in an unperturbed slow solar wind (*1*), in the region of interaction and compression in front of a magnetic cloud (*2*), and in the magnetic cloud (*3*). The dotted line corresponds to the prediction of the Kolmogorov turbulence model.

The energy transport in such systems can be described in the framework of models that include nonlocal transport and statistical distribution in the system [87–89, 112, 113]. Violation of Taylor's hypothesis is also possible because the inherent phase velocity of plasma waves cannot always be disregarded at the relevant frequencies [114].

Furthermore, substantial variations in the characteristic frequencies of the slope break and spectral slopes, and also the presence of non-power-law spectra (local peaks or flattening) are typical of any locally observed (nonaveraged) spectra [105, 106]. The strongest deviations in the spectral characteristics from the model prediction are observed on kinetic scales. In fact, this can be interpreted as the absence of local balance between the input and downscale spectral energy fluxes. As an example, Fig. 11 compares spectra of ion stream fluctuations at scales of 0.02–10 Hz for successive intervals of slow solar wind (stationary medium), the compression region in front of a magnetic

cloud (region of intense interaction of two streams), and the region of the magnetic cloud (a relatively quiet core of perturbation originating from the solar corona). All three spectra are substantially different from the classical spectrum of ion stream fluctuations (see Fig. 10). In the interaction region, the intensity of fluctuations increases, whereas the spectrum becomes noticeably steeper at both inertial and dissipation scales. In the inertial range, the spectrum corresponds to the Kolmogorov law with the exponent $-5/3$ only in the cloud, whereas the spectrum is 'flatter' in the calm wind and steeper in the interaction region. The minimum slope can be interpreted as the absence of pumping (large amplitudes on large scales, on the left side of the spectrum).

A classical transition from the inertial range to the dissipation range is observed only for slow stationary wind, whereas in the perturbed intervals a spectral flattening is observed under the transition between different scales, which may be due to a combination of Alfvén and kinetic Alfvén turbulence in the case of a small ratio of the thermal plasma pressure to the magnetic pressure [115].

For the dissipation range, the spectral exponents that are closest to the value $-7/3$ predicted by the theory of kinetic Alfvén turbulence [108] are observed for a quiet solar wind. In the perturbed regions, the spectra steepen noticeably, reaching a maximum (in absolute value) of -3.7 in the stream interaction region (see also [116]). A steeper-than-classical spectral slope correlates with the stronger level of fluctuation power [117, 118] and implies higher plasma heating rates [119].

These results allow us to draw the conclusion that free development of turbulence in the solar wind is nevertheless subject to the effect of boundaries between large-scale solar wind streams. The use of specialized spectrometers with high temporal resolution opens new horizons for exploring plasma turbulent fluctuations on kinetic scales. Further development of this activity is planned in future Russian space projects.

5. Conclusions

The solar wind is a unique natural phenomenon allowing us to learn more about the Sun as a star and also about the dynamics of collisionless plasma in space. On the other hand, studies and monitoring of the interplanetary medium are important for solving the practical problem of space weather forecasting. Even though the plasma of the solar wind seems to be a simple object, even in this case the results of direct measurement indicate that theoretical models need substantial improvements. This is why scientific programs of space agencies devote considerable attention to experiments with solar wind. For example, the projects Parker Solar Probe (USA, 2018), Solar Orbiter (Europe, 2020), Interheliosonde (Russia, 2026), Resonance-MKA (Russia, 2023), Luna-Resurs (Russia, 2024) have either been launched very recently or are in preparation to be launched.

References

1. Hundhausen A J *Coronal Expansion and Solar Wind* (Berlin: Springer-Verlag, 1972)
2. Schwenn R, in *Solar Wind Five. Proc. of a Conf., Woodstock, Vermont, November 1–5, 1982* (NASA Conf. Publ., 2280, Ed. M Neugebauer) (Washington, DC: NASA, 1983) p. 489
3. Neugebauer M *Space Sci. Rev.* **33** 127 (1982)
4. Cranmer S R, Winebarger A R *Annu. Rev. Astron. Astrophys.* **57** 157 (2019)
5. Sheeley N R (Jr.), Harvey J W, Feldman W C *Solar Phys.* **49** 271 (1976)
6. Kilpua E K J et al. *Geophys. Res. Lett.* **42** 3076 (2015)
7. Richardson J D, Kasper J C *J. Atmos. Sol. Terr. Phys.* **70** 219 (2008)
8. Yermolaev Yu I et al. *J. Geophys. Res. Space Phys.* **120** 7094 (2015)
9. McComas D J et al. *J. Geophys. Res.* **105** 10419 (2000)
10. McComas D J et al. *Geophys. Res. Lett.* **29** 1290 (2002)
11. Baker D N et al. *J. Geophys. Res.* **101** 12975 (1996)
12. McPherron R L, Russel C T, Aubry M P *J. Geophys. Res.* **78** 3131 (1973)
13. Gosling J T, Pizzo V J *Space Sci. Rev.* **89** 21 (1999)
14. Gonzalez W D et al. *J. Geophys. Res.* **99** 5771 (1994)
15. Bothmer V, Schwenn R *J. Geomagn. Geoelectr.* **47** 1127 (1995)
16. Veselovsky I S et al. *Cosmic Res.* **42** 435 (2004); *Kosmich. Issled.* **42** 453 (2004)
17. Yermolaev Y I, Yermolaev M Y *Geophys. Res. Lett.* **35** L01101 (2008)
18. Hapgood M A *Planet. Space Sci.* **40** 711 (1992)
19. Balogh A, Erdős G *Space Sci. Rev.* **176** 177 (2013)
20. Hoeksema J T *Space Sci. Rev.* **72** 137 (1995)
21. Wang Y-M et al. *Astrophys. J.* **488** L51 (1997)
22. Gringauz K I et al. *Sov. Phys. Dokl.* **5** 361 (1960); *Dokl. Akad. Nauk SSSR* **131** 1301 (1960)
23. Parker E N *Astrophys. J.* **128** 664 (1958)
24. Mursula K, Hiltula T *Solar Phys.* **224** 133 (2004)
25. Wilcox J M, Hoeksema J T, Scherrer P H *Science* **209** 603 (1980)
26. Israelevich P L et al. *Astron. Astrophys.* **376** 288 (2001)
27. Bavassano B, Woo R, Bruno R *Geophys. Res. Lett.* **24** 1655 (1997)
28. Wang Y-M et al. *Astrophys. J.* **498** L165 (1998)
29. Wilcox J M, Scherrer P H *J. Geophys. Res.* **77** 5385 (1972)
30. Hoeksema J T, Wilcox J M, Scherrer P H *J. Geophys. Res.* **88** 9910 (1983)
31. Riley P, Linker J A, Mikić Z *J. Geophys. Res.* **107** 1136 (2002)
32. Antonucci E, Svalgaard L *Solar Phys.* **36** 115 (1974)
33. Burlaga L F, Ness N F *J. Geophys. Res.* **102** 19731 (1997)
34. Balogh A *Space Sci. Rev.* **83** 93 (1998)
35. Smith E J et al. *Geophys. Res. Lett.* **20** 2327 (1993)
36. Schatten K H, Wilcox J M, Ness N F *Solar Phys.* **6** 442 (1969)
37. Levine R H, Schulz M, Frazier E N *Solar Phys.* **77** 363 (1982)
38. Arge C N, Pizzo V J *J. Geophys. Res.* **105** 10465 (2000)
39. Wang Y-M, Young P R, Muglach K *Astrophys. J.* **780** 103 (2014)
40. Maiewski E V et al. *Plasma Phys. Rep.* **44** 80 (2018); *Fiz. Plazmy* **44** 89 (2018)
41. Parker E N *Astrophys. J.* **139** 72 (1964)
42. Stewart G A, Bravo S *J. Geophys. Res.* **102** 11263 (1997)
43. Banaszkiewicz M, Axford W I, McKenzie J F *Astron. Astrophys.* **337** 940 (1998)
44. Burger R A et al. *Astrophys. J.* **674** 511 (2008)
45. Owens M J, Crooker N U, Lockwood M *J. Geophys. Res. Space Phys.* **119** 36 (2014)
46. Khabarova O V et al. *Astrophys. J.* **836** 108 (2017)
47. Izmodenov V V *Phys. Usp.* **61** 793 (2018); *Usp. Fiz. Nauk* **188** 881 (2018)
48. Quémerais E et al. *J. Geophys. Res.* **111** A09114 (2006)
49. Katushkina O A et al. *J. Geophys. Res. Space Phys* **118** 2800 (2013)
50. Katushkina O et al. *Solar Phys.* **294** 17 (2019)
51. Koutroumpa D et al. *Geophys. Res. Lett.* **46** 4114 (2019)
52. Tokumaru M, Kojima M, Fujiki K *J. Geophys. Res.* **117** A06108 (2012)
53. Crooker N U et al. *J. Geophys. Res.* **87** 2224 (1982)
54. Russell C T, Siscoe G L, Smith E J *Geophys. Res. Lett.* **7** 381 (1980)
55. Petrukovich A A et al. *J. Atmos. Sol. Terr. Phys.* **63** 1643 (2001)
56. Perreault P, Akasofu, S I *Geophys. J. Int.* **54** 547 (1978)

57. Podladchikova T V, Petrukovich A A *Space Weather* **10** S07001 (2012)
58. Podladchikova T, Petrukovich A, Yermolaev Y *J. Space Weather Space Clim.* **8** A22 (2018)
59. Burton R K, McPherron R L, Russell C T *J. Geophys. Res.* **80** 4204 (1975)
60. O'Brien T P, McPherron R L *J. Atmos. Sol. Terr. Phys.* **62** 1295 (2000)
61. Barkhatov N A, Dolgova D S, Revunova E A *Geomagn. Aeron.* **59** 16 (2019); *Geomagn. Aeron.* **59** 19 (2019)
62. Tsurutani B T, Ho C M *Rev. Geophys.* **37** 517 (1999)
63. Hudson P D *Planet. Space Sci.* **18** 1611 (1970)
64. Söding A et al. *Ann. Geophys.* **19** 667 (2001)
65. Vasquez B J et al. *J. Geophys. Res.* **112** A11102 (2007)
66. Horbury T S et al. *Geophys. Res. Lett.* **28** 677 (2001)
67. Neugebauer M *J. Geophys. Res.* **111** A04103 (2006)
68. Kennel C F et al. *JETP Lett.* **48** 79 (1988); *Pis'ma Zh. Eksp. Teor. Fiz.* **48** 75 (1988)
69. Malkov M A et al. *Phys. Fluids B* **3** 1407 (1991)
70. Medvedev M V et al. *Phys. Plasmas* **4** 1257 (1997)
71. Osman K T et al. *Phys. Rev. Lett.* **111** 201101 (2013)
72. Servidio S et al. *J. Plasma Phys.* **81** 325810107 (2015)
73. Escoubet C P, Fehringer M, Goldstein M *Ann. Geophys.* **19** 1197 (2001)
74. Greco A et al. *Astophysic. J. Lett.* **823** L39 (2016)
75. Podesta J J *J. Geophys. Res. Space Phys.* **122** 2795 (2017)
76. Vasko I Y et al. *Ann. Geophys.* **32** 1349 (2014)
77. Harrison M G, Neukirch T *Phys. Rev. Lett.* **102** 135003 (2009)
78. Allanson O et al. *J. Plasma Phys.* **82** 905820306 (2016)
79. Angelopoulos V *Space Sci. Rev.* **165** 3 (2011)
80. Burch J L et al. *Space Sci. Rev.* **199** 5 (2016)
81. Artemyev A V et al. *Geophys. Res. Lett.* **46** 1185 (2019)
82. Bobrova N A, Syrovatskii S I *JETP Lett.* **30** 535 (1979); *Pis'ma Zh. Eksp. Teor. Fiz.* **30** 567 (1979)
83. Medvedev M V et al. *Phys. Rev. Lett.* **78** 4934 (1997)
84. Zelenyi L M, Milovanov A V *Phys. Usp.* **47** 749 (2004); *Usp. Fiz. Nauk* **174** 809 (2004)
85. Zelenyi L, Artemyev A, Petrukovich A *Space Sci. Rev.* **188** 287 (2015)
86. Zhuravleva I et al. *Nature* **515** 85 (2014)
87. Budaev V P, Savin S P, Zelenyi L M *Phys. Usp.* **54** 875 (2011); *Usp. Fiz. Nauk* **181** 905 (2011)
88. Budaev V P, Zelenyi L M, Savin S P *J. Plasma Phys.* **81** 395810602 (2015)
89. Bruno R, Carbone V *Living Rev. Solar Phys.* **10** 2 (2013)
90. Cranmer S R et al. *Philos. Trans. R. Soc. Lond. A* **373** 20140148 (2015)
91. Matthaeus W H, Velli M *Space Sci. Rev.* **160** 145 (2011)
92. Taylor G I *Proc. R. Soc. Lond. A* **164** 476 (1938)
93. Bavassano B *Space Sci. Rev.* **78** 29 (1996)
94. Borovsky J E *J. Geophys. Res.* **113** A08110 (2008)
95. Gary S P *Philos. Trans. R. Soc. London A* **373** 20140149 (2015)
96. Alexandrova O et al. *Space Sci. Rev.* **178** 101 (2013)
97. Unti T W J, Neugebauer M, Goldstein B E *Astrophys. J.* **180** 591 (1973)
98. Smirnov V N, Vaisberg O L *Adv. Space Res.* **15** 297 (1995)
99. Zastenker G N et al. *Cosmic Res.* **51** 78 (2013); *Kosmich. Issled.* **51** 88 (2013)
100. Šafránková J et al. *Space Sci. Rev.* **175** 165 (2013)
101. Zelenyi L M et al. *Cosmic Res.* **51** 73 (2013); *Kosmich. Issled.* **51** 83 (2013)
102. Šafránková J et al. *Astrophys. J.* **803** 107 (2015)
103. Šafránková J et al. *Astrophys. J.* **825** 121 (2016)
104. Riazantseva M O et al. *Philos. Trans. R. Soc. Lond. A* **373** 20140146 (2015)
105. Riazantseva M O et al. *J. Plasma Phys.* **83** 705830401 (2017)
106. Rakhmanova L et al. *J. Geophys. Res. Space Phys.* **123** 5300 (2018)
107. Frisch U *Turbulence. The Legacy of A.N. Kolmogorov* (Cambridge: Cambridge Univ. Press, 1995); Translated into Russian: *Turbulentnost'. Nasledie Kolmogorova* (Moscow: FAZIS, 1998)
108. Schekochihin A A et al. *Astrophys. J. Suppl.* **182** 310 (2009)
109. Boldyrev S, Perez J C *Astrophys. J. Lett.* **758** L44 (2012)
110. Howes G G et al. *J. Geophys. Res.* **113** A05103 (2008)
111. Markovskii S A, Vasquez B J, Smith C W *Astrophys. J.* **675** 1576 (2008)
112. Marsch E, Tu C-Y *Nonlin. Processes Geophys.* **4** 101 (1997)
113. Salem C et al. *Astrophys. J.* **702** 537 (2009)
114. Klein K G, Howes G G, TenBarge J M *Astrophys. J. Lett.* **790** L20 (2014)
115. Chandran B D G et al. *Astrophys. J.* **707** 1668 (2009)
116. Riazantseva M O et al. *Geomagn. Aeron.* **59** 127 (2019); *Geomagn. Aeron.* **59** 127 (2019)
117. Smith C W et al. *Astrophys. J.* **645** L85 (2006)
118. Bruno R, Trenchi L, Telloni D *Astrophys. J. Lett.* **793** L15 (2014)
119. Leamon R J et al. *J. Geophys. Res.* **103** 4775 (1998)